====================
MATHEMATICAL
PHYSICS
====================

Simulation of the Laminar–Turbulent Transition by Applying Dissipative Numerical Schemes

I. V. Egorov[a,b], N. C. Nguyen[a,*], T. S. Nguyen[c], and P. V. Chuvakhov[a,b]

[a] *Moscow Institute of Physics and Technology (National Research University), Dolgoprudnyi, Moscow oblast, 141701 Russia*
[b] *Central Aerohydrodynamic Institute (TsAGI), National Research Center "Zhukovsky Institute", Zhukovskii, Moscow oblast, 140180 Russia*
[c] *Hanoi Industrial University, Hanoi, Vietnam*
*e-mail: nguyennhucan528@gmail.com

Abstract—The applicability of a low-order monotone shock-capturing scheme to the simulation of the laminar–turbulent transition is demonstrated. The laminar–turbulent transition is simulated in a supersonic boundary layer over a flat plate at a Mach number of 3. The numerical results are compared with results of other authors based on low-dissipative schemes. The spectral characteristics of disturbances in the linear and nonlinear development regions, the structure of the transient flow, and averaged boundary layer characteristics are compared.

1. INTRODUCTION

Modern aircraft design relies on results of aerodynamic research. An experimental study is usually associated with high financial costs of setting up and carrying out experiments in wind tunnels, while resulting experimental data are limited. In contrast to experiments, numerical simulation of unsteady compressible gas flows allows one to study flows over bodies of arbitrary configuration, to reveal the fine structure of observed phenomena, and to obtain results that are difficult to produce experimentally. Simulation results are used to calculate aerodynamic and thermodynamic characteristics, such as the pressure, friction, and heat transfer coefficients. The last characteristic is of crucial importance at high supersonic and hypersonic flow speeds, in particular, when the boundary-layer flow undergoes turbulization and the friction and heat transfer coefficients to the surface increase by several times.

Wind tunnel data on the position of the laminar–turbulent transition (LTT) vary, since they depend on the background of disturbances in the flow through a particular tunnel. That is why the direct numerical simulation of flows in the LTT regime is of special value, since this background can be strictly controlled. Unfortunately, for practically important regimes, the space and time costs of such simulations are too high. High-performance multiprocessor computer clusters (supercomputers) make it possible to perform only local computations aimed at the study of linear and nonlinear mechanisms underlying LTT. The computational costs can be reduced by applying numerical schemes of low order of accuracy.

Monotone shock-capturing schemes are dissipative. As a result, they are suitable for stable computation of flows with shock waves, separation regions, boundary layers, and other flow features, taking into account their interaction. Excessive dissipation leads to the numerical decay of small disturbances. However, the growth rate of disturbances in unstable boundary layers can noticeably exceed the effects associated with numerical dissipation. In this work, a monotone scheme of second-order accuracy in space and time is successfully used to simulate LTT in a supersonic boundary layer over a flat plate at a Mach number of 3. The simulation results are compared with their counterparts produced by a much less dissipative method [1] based on a fourth-order accurate scheme in the streamwise and normal directions and the spectral method in the spanwise direction; the time stepping relies on the fourth-order Runge–Kutta method. The present study was started in [2]. In contrast to [2], the spectral characteristics of disturbances in the linear and nonlinear development regions and integral flow characteristics are compared in detail.

2. FORMULATION OF THE PROBLEM

2.1. Brief Description of the Numerical Method

In this work, the solver HSFlow++ [3] is used for direct numerical simulation of flows based on the Navier–Stokes equations. The differential equations are written in a curvilinear coordinate system (ξ, η, ζ) in dimensionless conservative form:

$$\frac{\partial \mathbf{Q}}{\partial t} + \frac{\partial \mathbf{E}}{\partial \xi} + \frac{\partial \mathbf{G}}{\partial \eta} + \frac{\partial \mathbf{F}}{\partial \zeta} = 0.$$

The equations are solved numerically in dimensionless variables. The Cartesian coordinates $x^* = xL$, $y^* = yL$, and $z^* = zL$ are normalized by the characteristic length L; the time $t^* = tL/V_\infty$, by the characteristic time L/V_∞; the velocity components $u^* = uV_\infty$, $v^* = vV_\infty$, and $w^* = wV_\infty$, by the free-stream speed V_∞; the pressure $p^* = p(\rho_\infty V_\infty^2)$, by the doubled free-stream dynamic pressure; and the other gasdynamic variables, by their free-stream values. Dimensional variables are denoted by a star superscript. Variables with no star are supposed to be dimensionless. The symbol ∞ denotes free-stream values.

The differential equations are approximated using a fully implicit finite volume method and a second-order accurate scheme in time:

$$\frac{3\mathbf{Q}_{i,j,k}^{n+1} - 4\mathbf{Q}_{i,j,k}^{n} + \mathbf{Q}_{i,j,k}^{n-1}}{\Delta t} + \frac{\mathbf{E}_{i+\frac{1}{2},j,k}^{n+1} - \mathbf{E}_{i-\frac{1}{2},j,k}^{n+1}}{h_\xi} + \frac{\mathbf{G}_{i,j+\frac{1}{2},k}^{n+1} - \mathbf{G}_{i,j-\frac{1}{2},k}^{n+1}}{h_\eta} + \frac{\mathbf{F}_{i,j,k+\frac{1}{2}}^{n+1} - \mathbf{F}_{i,j,k-\frac{1}{2}}^{n+1}}{h_\zeta} = 0.$$

Convective fluxes on cell faces (e.g., $\mathbf{E}_{i+1/2,j,k}^{n+1}$) are determined using dimensional splitting. In each direction, we find the Jacobian matrix ($A = \partial\mathbf{E}/\partial\mathbf{Q}$ in the ξ direction), which is diagonalized in the form $A = B\Lambda B^{-1}$, where B is the matrix made up of the right eigenvectors of A and Λ is a diagonal matrix whose elements are the eigenvalues of A. The convective components of the fluxes $\mathbf{E}$, $\mathbf{G}$, and $\mathbf{F}$ on cell faces are approximated using a monotone Godunov-type scheme:

$$\mathbf{E}_{i+\frac{1}{2}} = \frac{1}{2}[\mathbf{E}(\mathbf{Q}_L) + \mathbf{E}(\mathbf{Q}_R) - B_{LR}\Lambda(\varphi(\lambda_{LRi}))B_{LR}^{-1}(\mathbf{Q}_R - \mathbf{Q}_L)],$$

where the subscripts L and R denote quantities computed on the right and left sides of the considered face with the use of gasdynamic variables recovered by applying a reconstruction procedure. For example, for face $i + 1/2$, the index L corresponds to cell i, while the index R, to cell $i + 1$. The subscript LR denotes quantities computed using the Roe method for the approximate solution of the Riemann problem. A physically correct variation in entropy at discontinuities is ensured by modifying the eigenvalues $\varphi(\lambda)$. The reconstruction procedure is based on the WENO-3 method.

The diffusion components of the vectors $\mathbf{E}$, $\mathbf{G}$, and $\mathbf{F}$ on faces of elementary cells are approximated by applying a second-order accurate central-difference scheme:

$$\left.\frac{\partial q}{\partial \xi}\right|_{i+\frac{1}{2},j,k} = \frac{1}{h_\xi}(q_{i+1,j,k} - q_{i,j,k}),$$

$$\left.\frac{\partial q}{\partial \eta}\right|_{i+\frac{1}{2},j,k} = \frac{1}{4h_\eta}(q_{i+1,j+1,k} + q_{i,j+1,k} - q_{i+1,j-1,k} - q_{i,j-1,k}),$$

$$\left.\frac{\partial q}{\partial \zeta}\right|_{i+\frac{1}{2},j,k} = \frac{1}{4h_\zeta}(q_{i+1,j,k+1} + q_{i,j,k+1} - q_{i+1,j,k-1} - q_{i,j,k-1}),$$

where q is any of the nonconservative (primitive) dependent variables u, v, w, p, or T of the problem.

After approximating the Navier–Stokes equations and the boundary conditions, the integration of the original partial differential equations is reduced to solving a system of nonlinear algebraic equations $R(\mathbf{U}) = 0$, where R is a discretization operator computing the residual vector based on the approximation of the equations and $\mathbf{U}$ is the vector of desired nonconservative variables (u, v, w, p, T) (velocity components, pressure, and temperature) at all grid nodes. The length of the vector $\mathbf{U}$ is $n_q N$, where N is the total number of grid nodes, including boundary ones and n_q is the number of unknowns at each node

($n_q = 5(u, v, w, p, T)$ and $n_q = 4(u, v, p, T)$ in the three- and two-dimensional formulations, respecively). The system of discrete equations $R(\mathbf{U}) = 0$ is solved using the modified Newton–Raphson method

$$\mathbf{U}^{[k+1]} = \mathbf{U}^{[k]} - \tau^{[k+1]}(J^{[k_0]})^{-1}R(\mathbf{U}^{[k]}),$$

where k and k_0 are iteration numbers with respect to nonlinearity ($k_0 \leq k$), $J^{[k_0]} = (\partial R/\partial \mathbf{U})^{[k_0]}$ is the Jacobian matrix of the system of nonlinear equations, $R(\mathbf{U}^{[k]})$ is the residual vector, and τ is the regularization parameter. Here, the expression $(J^{[k_0]})^{-1}R(\mathbf{U}^{[k]}) \equiv Y^{[k]}$ is the solution to the linear system of equations

$$(J^{[k_0]})Y^{[k]} = R(\mathbf{U}^{[k]}).$$

The regularization parameter of Newton's method with respect to the initial approximation $\tau^{[k]}$ is determined by the formula

$$\tau^{[k+1]} = \frac{(Y^{[k]} - Y^{[k-1]})Y^{[k]}}{(Y^{[k]} - Y^{[k-1]})^2}.$$

With the convergence of the iterative process, we have $\tau^{[k]} \to 1$ and the convergence rate theoretically tends to a quadratic one.

Since the considered numerical scheme includes solving the Riemann problem, an analytical form of the corresponding Jacobian matrix J is difficult to obtain. In the present solver, the matrix $J^{[k_0]} = (\partial R/\partial \mathbf{U})^{[k_0]}$ is formed at the nonlinear iteration k_0 by applying the universal method of finite increments of the residual vector R with respect to the vector of desired variables $\mathbf{U}$. Here, the mth column of the matrix $J^{[k_0]}$ is computed as

$$J_m^{[k_0]} = \frac{R(\mathbf{U}^{[k_0]} + \varepsilon e_m) - R(\mathbf{U}^{[k_0]})}{\varepsilon}, \quad \varepsilon = 10^{-8}, \quad m = 1, \ldots, n_q N,$$

where $\mathbf{e}_m$ is the $n_q N$-dimensional unit vector consisting of 0's, except for the only 1 in position m. This technique for computing the Jacobian is applicable to an arbitrary system of discrete equations.

2.2. Flow Parameters and Formulation of the Problem

We considered the formally two-dimensional flow over a sharp flat plate at the free-stream Mach number $M_\infty = 3$ and the free-stream temperature $T_\infty = 103.6$ K. The evolution of disturbances was computed in a subdomain. The computation procedure was similar to the one described in [4]. The Reynolds number was $\mathrm{Re}_{1,\infty} = 2.181 \times 10^6$ m^{-1}. The Prandtl number was set to a constant: $\mathrm{Pr} = \mu c_p/\lambda = 0.71$. The Navier–Stokes equations were closed by the equation of state $\gamma M_\infty^2 p = \rho T$, where $\gamma = 1.4$ is the ratio of specific heats. The dynamic molecular viscosity was calculated according to Sutherland's law: $\mu = (1 + T_\mu)/(T + T_\mu)T^{3/2}$, where $T_\mu = T_\mu^*/T_\infty^* = 110.4$ K$/103.6$ K ≈ 1.07.

The numerical integration was carried out in the rectangular domain shown in Fig. 1. At inlet and upper boundaries, we set the dimensionless free-stream parameters $(u, v, w, p, T) = (1, 0, 0, 1/\gamma M_\infty^2, 1)$. For steady computations, the wall was assumed to be heat-insulated with no-slip conditions specified on it. The outlet boundary was preceded by a buffer zone with enlarged cells in x and y for damping disturbances going out through the boundary. At the outlet boundary, we set mild conditions, such as linear extrapolation of primitive variables from the computational domain. Symmetry conditions were specified at the lateral boundaries z_{min} and z_{max}.

The computation was performed as follows. First, the two-dimensional steady unperturbed flow over the flat plate was computed until the residual reached a value of 10^{-8}. Second, a subdomain for the subsequent simulation of the evolution of disturbances was cut out of the resulting solution. The gasdynamic quantities obtained at the first step were fixed at the new inlet boundaries of the subdomain. A steady field was established additionally until complete convergence (the residual value did not exceed 10^{-8}). Third, the steady field obtained in the subdomain was duplicated in the third (spanwise) direction z. The surface temperature distribution was *fixed*. Disturbances of the blowing–suction type were introduced into the boundary layer as described below. Unsteady computations were performed until a quasi-steady flow
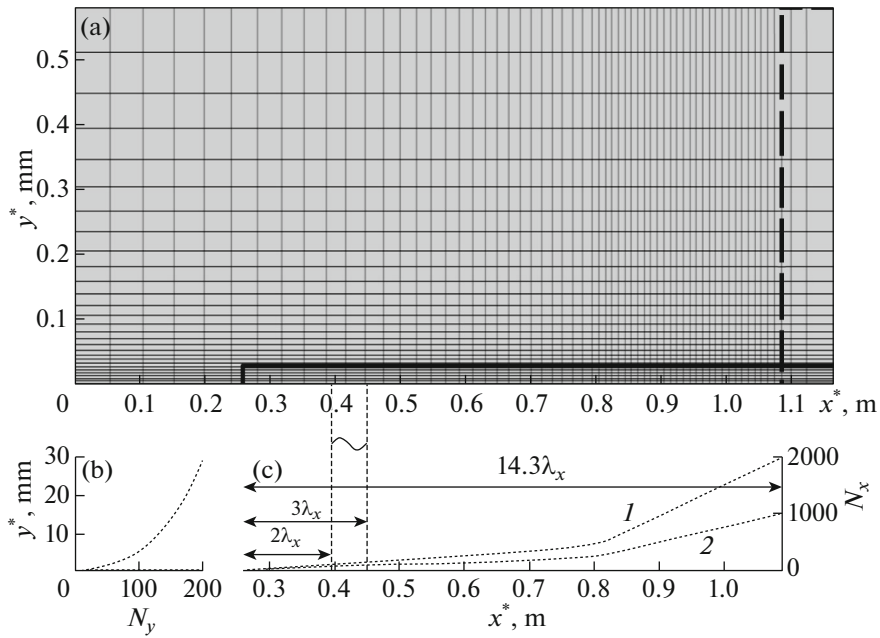
Fig. 1. Problem formulation: (a) computational domain and grid (every 10th grid line is shown); (b) mesh refinement in the normal direction to the wall; and (c) mesh refinement in the longitudinal direction: grids consisting of (*1*) 80 million nodes and (*2*) 20 million nodes.

regime was established. In the case of this approach, the surface of the plate was adiabatic, but temperature fluctuations on the surface were absent.

2.3. Source of Disturbances

Following [1], a source of disturbances is modeled for $x^* \in [x_1^*, x_2^*] = [0.394, 0.452]$ m. In this range, the normal velocity has the form

$$v(x, y = 0, t) = A(t)v_p(x_p)\cos(\beta_0 z)\cos(-\omega_0 t),$$

where

$$v_p = \begin{cases} 1.5^4(1 + x_p)^3(3(1 + x_p)^2 - 7(1 + x_p) + 4), & -1 \le x_p \le 0, \\ -1.5^4(1 - x_p)^3(3(1 - x_p)^2 - 7(1 - x_p) + 4), & 0 \le x_p \le 1, \end{cases} \quad x_p = \frac{2x - (x_2 + x_1)}{x_2 - x_1},$$

$$A(t) = \varepsilon \begin{cases} 0, & t < 0, \\ 0.1^{((T-t)/(0.9T))^2}, & 0 \le t \le T, \\ 1, & t > T, \end{cases}$$

where $T = 2\pi/\omega$, $A(t)$ is the amplitude and $\varepsilon = 0.00573$. The other flow parameters near the source are computed as in the case of a wall with no source. The disturbance at the frequency $\omega_0^*/2\pi = f_0^* = 6.36$ kHz with the wave number $\beta_0^* = 211.52$ m^{-1} is called fundamental.

As will be shown later, the present results agree well both qualitatively and quantitatively with those of [1]. However, the disturbance amplitude ε in this work is nearly twice as large as in [1] (where $\varepsilon = 0.003$) and is chosen so that the positions of the LTT onset coincide. As will be shown below, numerical dissipation does not affect the position of LTT in this work. Possibly, this is why the disturbance amplitude in [1] was indicated incorrectly.

2.4. Numerical Grid

The characteristic length scale is specified as $L = 0.7239$ m. The streamwise size of the buffer zone, which is bounded by the dashed rectangle in Fig. 1, is equal to $1.5\lambda_x$, where $\lambda_x = x_2^* - x_1^*$ is the wavelength of the fundamental disturbance.

Figure 1 shows the computational domain and the grid (side view). The subdomain for basic unsteady computations is bounded by the solid rectangle and begins at a distance of $x_0^* = 0.258$ m from the leading edge of the plate. The length of the subdomain is 14.3 times larger than the streamwise wavelength of the fundamental disturbance. The height of the subdomain is specified as $y_H^* = 0.03$ m, which is at least five times the local boundary-layer thickness at the outlet boundary. The size of the subdomain in the lateral direction is one wavelength λ_z in the spanwise direction, where $\lambda_z = 2\pi/\beta_0^* \approx 0.0297$ m.

The grid is presented in Fig. 1a, and the corresponding grid refinements are shown in Figs. 1b and 1c. The basic computations in this work were carried out on a grid consisting of 80 million nodes (fine grid). This grid corresponds to the one in the $x0y$ plane in [1]. The grid lines are distributed uniformly in the spanwise direction. On the fine grid, the number of points in z is 201. The number of nodes in both x and z on the coarse grid is less by half than on the fine grid. In the vertical direction, both grids have an identical number of points. Across the boundary layer, there are at least 100 points. On the fine grid, the resolution of disturbances is 201 points per wavelength in the spanwise direction (in z) and 320 points per wavelength in the streamwise direction (in x). It should be noted that, for a monochromatic acoustic wave propagating in uniform flow, about 40 points per wavelength are required for achieving a nearly natural level of viscous wave attenuation for the used numerical method. Therefore, the numerical dissipation of the fundamental disturbance on the constructed grids is insignificant.

2.5. Analyzed Quantities

Data for processing and comparison were collected after establishing a quasi-periodic flow regime, namely, starting at the dimensionless time $t = 2.261$ after introducing disturbances into the boundary layer. The properties of the transient flow are analyzed in the next section.

The spectral content of disturbances was analyzed by comparing the amplitudes of individual Fourier harmonics or the maxima of these amplitudes in the normal direction to the surface in the considered cross section $x = $ const. Fourier analysis and processing of unsteady results were implemented in Python (library numpy). The results produced by the fast Fourier transform procedures in time and coordinate z were normalized by $N_t \times N_z/4$, where N_t and N_z are the numbers of points of the analyzed signal in time and coordinate z, respectively. In this work, we study the amplitudes of harmonics of fluctuations in streamwise velocity, pressure, temperature, and the maxima of these quantities in the normal direction to the surface.

The vortex structure of the flow fields were visualized using the Q-criterion $Q = 0.5(\Omega_{ij}\Omega_{ij} - S_{ij}S_{ij})$, where $S_{ij} = 0.5(\partial_j u_i + \partial_i u_j)$, $\Omega_{ij} = 0.5(\partial_j u_i - \partial_i u_j)$, and u_i are the velocity components (here, we used tensor notation with summation implied over repeated indices in products).

Additionally, we compared instantaneous fields of streamwise and spanwise vorticity and average flow parameters (skin friction coefficient and streamwise velocity profiles averaged in the sense of Favre and Reynolds).

3. ANALYSIS OF THE RESULTS

3.1. Flow Structures and Disturbance Spectrum

Figure 2 shows the instantaneous structure of the perturbed flow in terms of the Q-criterion. The source of disturbances is immediately followed by a region of linear development of disturbances, where they form X-shaped structures amplifying in the downstream direction. Near $x^* \approx 0.6$ mm, we can see the first signs of nonlinear interaction, namely, the disturbances become distorted. Intense nonlinear breakdown of disturbances is observed for $x^* \in (0.75, 0.85)$ m. Behind this region, there appears a zone of early turbulence with growing small-scale vortices. This zone develops in the downstream direction.

Since the exciting disturbances are periodic ones with a distinguished frequency and the nonlinear interactions lead to the generation of subharmonics, the response of the boundary layer to such disturbances also has to be periodic (quasi-steady flow regime). To study the spectral properties of LTT, the unsteady flow was first relaxed to a quasi-steady regime, and then statistic data were gathered within five

(a)

(b)
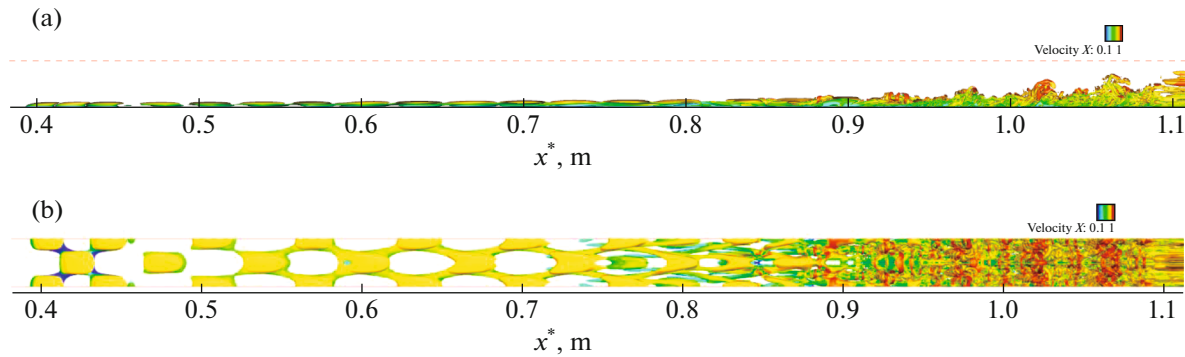
Fig. 2. Visualization of vortex structures in the boundary layer based on isosurfaces of the Q-criterion, $Q = 5$: (a) side view from $+z$ and (b) top view from $+y$. Color depicts the magnitude of the longitudinal velocity. The buffer zone begins at $x^* \approx 1.09$ m.

periods of this regime. An example of a quasi-steady signal at some point within the boundary layer is shown in Fig. 3a.

In each cross section $x^* = $ const, the disturbance can be represented as a sum of harmonic oscillations by applying the Fourier transform. For the considered flow over a flat plate, it is reasonable to perform the two-dimensional Fourier transform in time and spanwise coordinate for each line $x^* = $ const, $y^* = $ const. The result of this two-dimensional transform can be represented in the form of the amplitude of the harmonic $(f^*, \beta^*) = (h f_0^*, k \beta_0^*)$. Thus, the result of the two-dimensional Fourier transform can be represented in the form of amplitudes of two-dimensional harmonics $\hat{u}_{hk}$. Figure 3b shows an example for the beginning of the early turbulence region.

In the described problem formulation, the Fourier spectrum is symmetric, so only the spectral region for $h \geq 0$ and $k \geq 0$ is of interest. It should be noted that the spectral peaks represent a staggered pattern, which is explained by the quadratic (nonlinear) interaction of the disturbances. For example, for a steady disturbance, and other peaks are observed only at even wave numbers $k = 2, 4, 6, ...$ in the case of even frequencies $h = 0, 2, 4, ...$ and at odd wave numbers $k = 1, 3, 5, ...$ in the case of odd frequencies $h = 1, 3, 5, ...$. This pattern is typical of the oblique breakdown mechanism, when two harmonics with identical frequencies, but with oppositely signed wave numbers interact nonlinearly (quadratically). In this case, the frequency is doubled and the wave number is nullified: $[1, 1] + [1, -1] \rightarrow [2, 0]$. The closer the harmonic to the fundamental one, the higher is its amplitude. This is associated with the fact that the nonlinear breakdown gradually progresses into the high-frequency domain and with the numerical spatiotemporal dissipation of the used numerical method. The computations in this study were executed on two different grids, one being twice finer in the streamwise and spanwise directions. As will be shown later, the results obtained on both grids are similar.

Below, the present results are compared with those of [1].

3.2. Linear Regime

Consider the evolution of disturbances in the linear regime, which is observed from about $x^* = 0.4$ m to $x^* = 0.6$ m. In Fig. 4, the amplitudes of the fundamental mode $[1,1]$ of the streamwise velocity fluctuations u' at $x^* = 0.5$ m obtained in this work are compared with the results of [1]. Good agreement is observed for this case and for the other lines $x^* = $ const, $y^* = $ const (Figs. 4a–4c).

Among all possible lines $y^* = $ const in a given section $x^* = $ const, we can distinguish the line y_0^* on which the amplitude of the considered harmonic is maximal. For fluctuations u' or T', this line lies in the critical boundary layer, $y_0/\delta \approx 0.65$. The downstream evolution of this maximum agrees well with the results of [1] (Fig. 4d) even on the coarse grid.

As a characteristic of an unstable boundary layer, the growth rate of disturbances is sensitive to the structure of the steady solution. Consider the evolution of the streamwise disturbance growth rate for the streamwise velocity, $\alpha_i = -\dfrac{d}{dx}[\ln(u'_{max}(x))]$. Here, the subscript max denotes the maximum (in y) Fourier amplitude of the harmonic. Figure 5a demonstrates good agreement in the level of the growth rates in
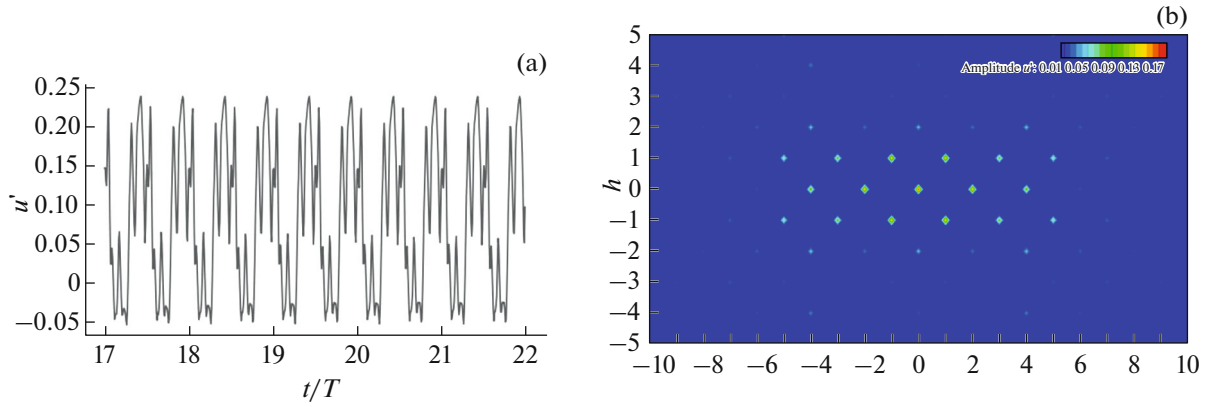
Fig. 3. (a) Quasi-stationary fluctuations of streamwise velocity, $u'(t, x_0^*, y_0^*, z_0^*)$, at the point $(x_0^*, y_0^*, z_0^*) = (0.9201, 0.0035, -0.0076)$; and (b) two-dimensional Fourier transform of the field $u'(t, x_0^*, y_0^*, z)$ on the line $(x_0^*, y_0^*) = (0.9201, 0.0035)$ m.
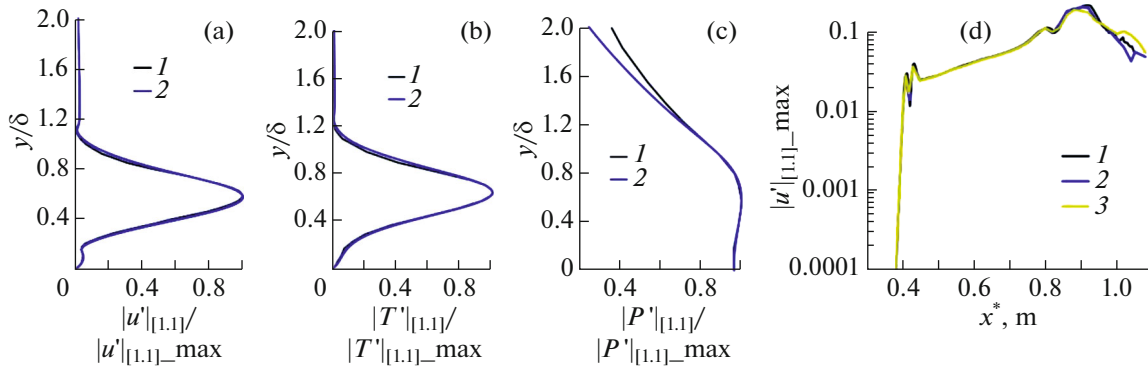
Fig. 4. Amplitudes of the harmonic [1, 1] for (a) $|u'_{[1,1]}|$, (b) $|T'_{[1,1]}|$, and (c) $|p'_{[1,1]}|$ in the cross section $x^* = 0.5$ m; and (d) the maximum (in y^*) amplitude of $|u'_{[1,1]}|$ as a function of x^*: (*1*) work [1], (*2*) fine grid (HSFlow++), and (*3*) coarse grid (HSFlow++).

cross sections $x =$ const. Starting at $x^* \approx 0.65$ m, the growth rate increases significantly. This moment corresponds to the beginning of the nonlinear stage in the disturbance development.

It should also be noted that good agreement is observed in the structure of disturbances within the boundary layer in various cross sections $y^* =$ const, which is demonstrated in Figs. 5b, 5c.

3.3. Nonlinear Regime

Consider the nonlinear stage of the disturbance development. The manifestation of the nonlinear interaction can be seen in the Q-criterion-based patterns, which exhibit a strengthening of the rope-like structures (Fig. 6). For small values of Q (15 and 100), our results agree well with those of [1]. However, in the early turbulence region, where there appear small-scale structures and the maximum value of Q grows (10000 and 40000), the dissipative scheme fails to perfectly reproduce the results of the low-dissipative scheme of [1]. The most probable cause of this discrepancy is the application of the spectral method in the spanwise direction in [1] and the use of high-frequency harmonics lying near the Nyquist frequency (wave number) for the used fine grid, which leads to their poor resolution.

Consider nonlinear breakdown via the evolution of the maximum (in y) amplitudes of disturbance harmonics. The oblique resonance mechanism develops sequentially. Initially, the most unstable fundamental oblique wave [1, ±1] grows, which is caused totally by the instability of the boundary layer. As a certain critical amplitude is attained, it begins to interact nonlinearly with itself, generating subharmonics: $h = 0$ and $h = 2$, $k = 0$, $k = 2$, which grow due to the nonlinear interaction of the fundamental harmonics.
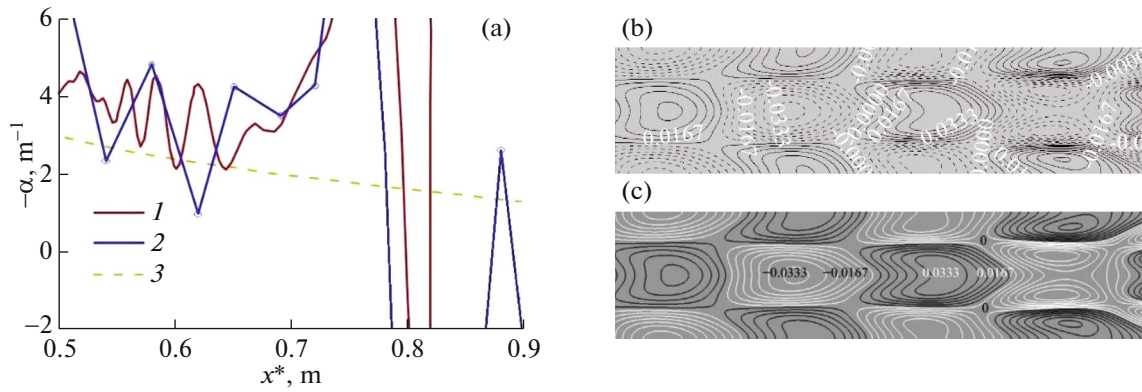
Fig. 5. (a) Streamwise growth rate of $|u'_{[1,1]}|$ based on the results of (*1*) [1], (*2*) present work (80 millions nodes), (*3*) linear stability theory (Mack code); (b), (c) the instantaneous contour of fluctuations u' in the cross section $x^* = 0.546{-}0.67$ m, $y^* = 2.3$ mm: (b) work [1], (c) fine grid.
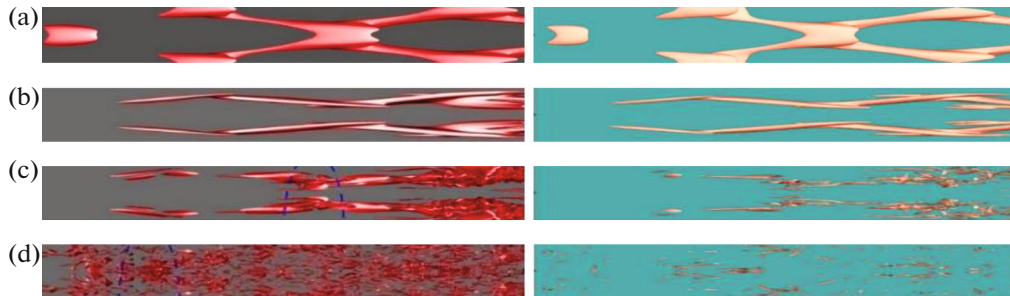

Fig. 6. Instantaneous isosurfaces of the Q-criterion, top view, based on the results of [1] (left panels) and of the present work, fine grid (right panels): (a) $Q = 15$, $x^* = 0.546{-}0.670$ m; (b) $Q = 100$, $x^* = 0.670{-}0.798$ m; (c) $Q = 10\ 000$, $x^* = 0.798{-}0.924$ m; and (d) $Q = 40\ 000$, $x^* = 0.924{-}1.051$ m.
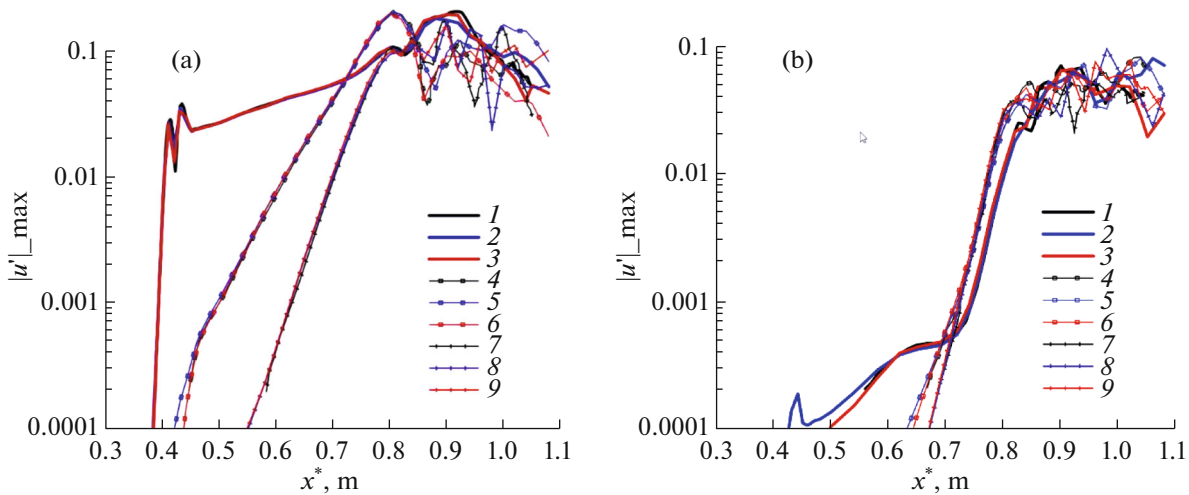

Fig. 7. Evolution of the maximum amplitude (in y) of the Fourier harmonic at odd frequencies for (a) $h = 1$ and (b) $h = 3$ (*1*), (*4*), (*7*) work [1]; (*2*), (*5*), (*8*) present work, coarse grid; (*3*), (*6*), (*9*) present work, fine grid; (*1*)–(*3*) $k = 1$; (*4*)–(*6*) $k = 3$; and (*7*)–(*9*) $k = 5$.

When the subharmonics reach sufficient amplitudes, they begin to interact nonlinearly with each other and with the fundamental harmonics, generating progressively more subharmonics. This process and its sequential stages in time can be seen in Figs. 7 and 8, which show the evolution of the harmonic ampli-
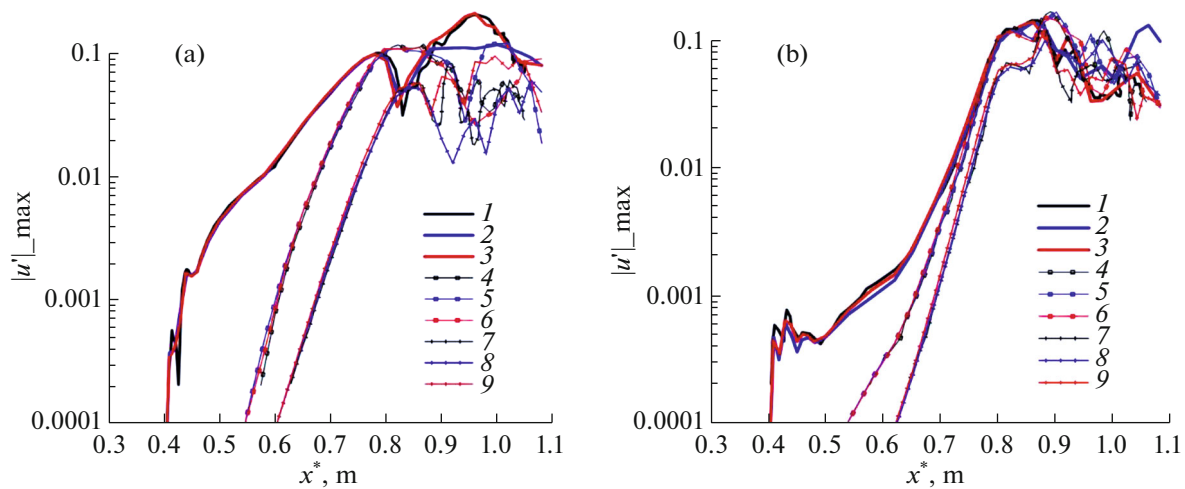
Fig. 8. The same as in Fig. 7, but at even frequencies for (a) $h = 0$ and (b) $h = 2$: (*1*)–(*3*) $k = 2$; (*4*)–(*6*) $k = 4$; and (*7*)–(*9*) $k = 6$.
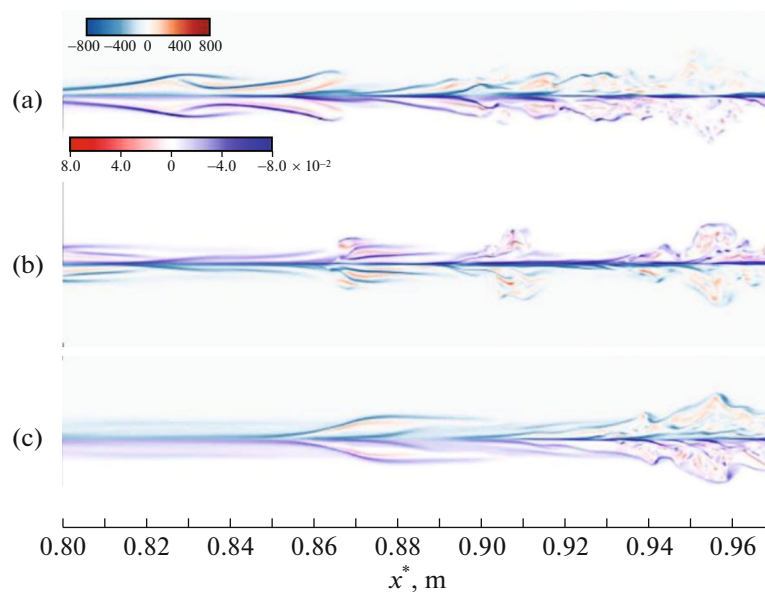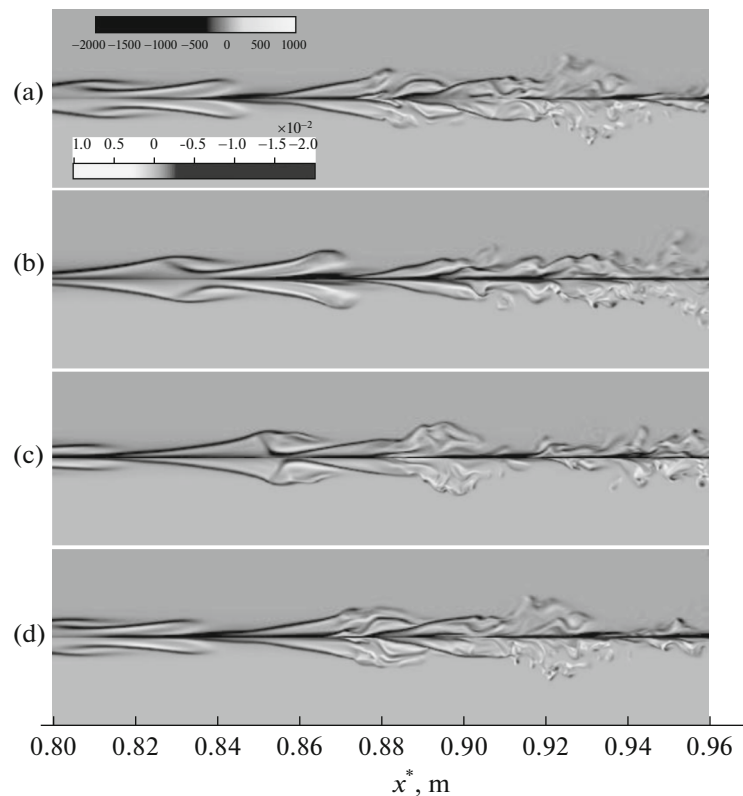

Fig. 9. Instantaneous field of spanwise vorticity at the time $t = 2.82891$ for (a) $z^* = -0.0092$ m, (b) $z^* = -0.0047$ m, and (c) $z^* = -0.0017$ m. The results of the present work, fine grid, and of [1] are shown in the upper and lower halves, respectively.

tudes in the downstream direction. The described mechanism explains the staggered structure of the spectrum presented in Fig. 3b.

It should be noted that the evolution of the harmonics agrees well with [1] in the domains of linear and weakly nonlinear development of disturbances. However, in the early turbulence region, the results obtained on the coarse grid begin to differ from their fine-grid counterparts. The latter still agree well with the results of [1] for the basic energy-containing frequencies $h = 0, 1$; $k = 1, 2$, and exhibit a small mismatch with growing h and k. Note that, in all cases, the Fourier amplitudes remain unchanged in value, but diverge in phase. This can be caused by the accumulation of the error of the more dissipative method. Overall, however, the described comparison of the results confirms the reliability and applicability of dissipative schemes for LTT simulation.

In Fig. 9, the instantaneous structures of spanwise vorticity in various cross sections $z^* = \text{const}$ obtained in this work (upper half of the figure) are compared with the results of [1] (mirrored in the lower

Fig. 10. Instantaneous field of the spanwise vorticity at the cross section $z^* = -0.0087$ m at various times: (a) $t = t_0$, (b) $t = t_0 + 6T/20$, (c) $t = t_0 + 12T/20$, and (d) $t = t_0 + 18T/20$. The results of the present work, fine grid, and of [5] are shown in the upper and lower halves, respectively.

half of the figure). It can be seen that small-scale structures typical of developed turbulence appear near $x^* = 0.865$ m. A detailed comparison shows that the vortices obtained in this work are less intense than those in [1] and contain fewer small-scale vortex structures, which was discussed above. The basic large-scale structures agree well with [1].

Now we consider a time visualization of the evolution of small-scale structures in a particular cross section $z = $ const. Figure 10 shows the instantaneous structures of spanwise vorticity computed at various times. They are compared with the results of [5], where the parameters of the problem coincide with those in [1], but the computations were performed on a fine grid consisting of 211 million nodes. Inspection of Fig. 10 suggests that the velocity of vortices propagating in the boundary layer is about 0.7.

Figure 10 also demonstrates the development of small-scale structures. The vortex at $x^* = 0.84$ m (Fig. 10a) moves through the point $x^* = 0.87$ m (Fig. 10b) and reaches the point $x^* = 0.9$ m (Fig. 10c), where it actively breaks up into small vortices, which are then carried away by the flow to $x^* = 0.92$ m (Fig. 10d). By this time, a new vortex has arrived at $x^* = 0.84$ m, and the process repeats (quasi-steady regime).

Once again, we note that the dissipative HSFlow++ scheme well reproduces large-scale structures, preserving them qualitatively and quantitatively. However, small-scale structures are reproduced insufficiently accurately, so they do not agree completely with the results of [5].

In Fig. 11, the computed instantaneous cross sections of streamwise vorticity are compared with the results of [1]. Since the flow structure is symmetric with respect to the plane $z^* = 0$, only a half of the domain in z^* is presented. A large vortex can be seen in the cross section $x^* = 0.862$ m (Fig. 11a). With increasing x, it grows and begins to break at $x^* = 0.866$ m (Fig. 11b), after which numerous small vortices are formed at the point $x^* = 0.870$ m (Fig. 11c). The vorticity fields produced by the dissipative numerical scheme (this work) agree well with the results of [1].
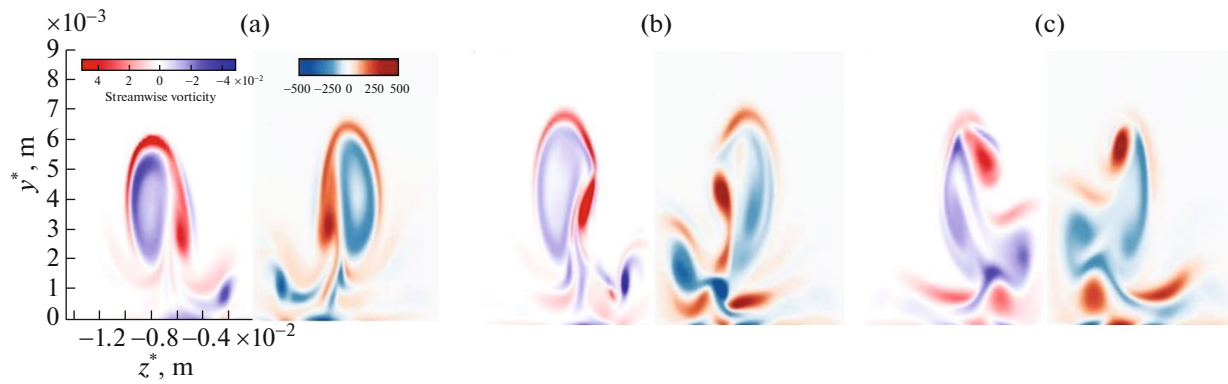
Fig. 11. Instantaneous streamwise vorticity at the time $t = 2.82891$ for (a) $x^* = 0.862$ m, (b) $x^* = 0.866$ m, and (c) $x^* = 0.870$ m. The left panel presents the results of [1], and the right panel depicts the results of the present work on the fine grid.
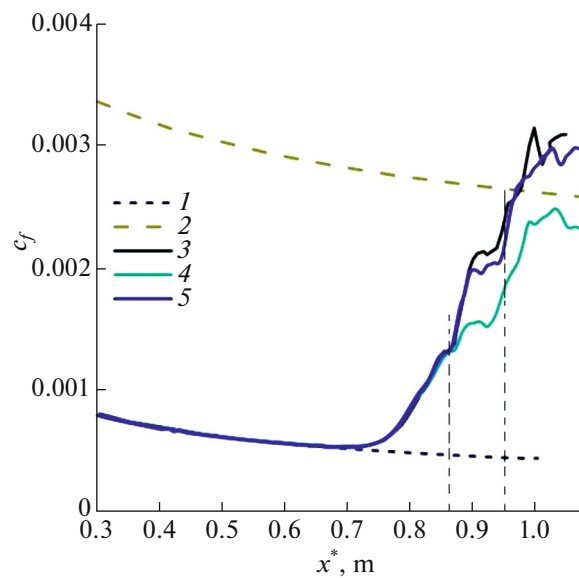
Fig. 12. Skin friction coefficient averaged in space and time: (*1*) laminar branch, (*2*) theoretical turbulent branch [6], (*3*) work [1], (*4*) present computation on the coarse grid, and (*5*) present computation on the fine grid.

Consider the averaged skin friction coefficient c_f as a function of the streamwise coordinate x. The local skin friction coefficient was computed using the formula

$$c_f = \frac{2}{\mathrm{Re}_\infty} \times \mu \left| \times \frac{\partial u}{\partial y} \right|_{y=0}.$$

In this work, the results were averaged in time over five fundamental periods $\Delta t = 10\pi/\omega_0$ and in z over the entire computational domain:

$$\overline{\varphi} = \frac{1}{\lambda_z} \frac{1}{\Delta t} \int\limits_0^{\lambda_z} \int\limits_{t_0}^{t_0 + \Delta t} \varphi(t, z) dt dz.$$

Starting at $x^* = 0.72$ m, the value of c_f increases sharply in the neighborhood of $x^* = 0.86$ m. In this region, the results produced by the dissipative scheme coincide with those of [1] even on the coarse grid. In the downstream region, the coarse-grid results are lower than their fine-grid counterparts. The latter agree satisfactorily with the results of [1] in the early turbulence region for $x^* \geq 0.9$ m.
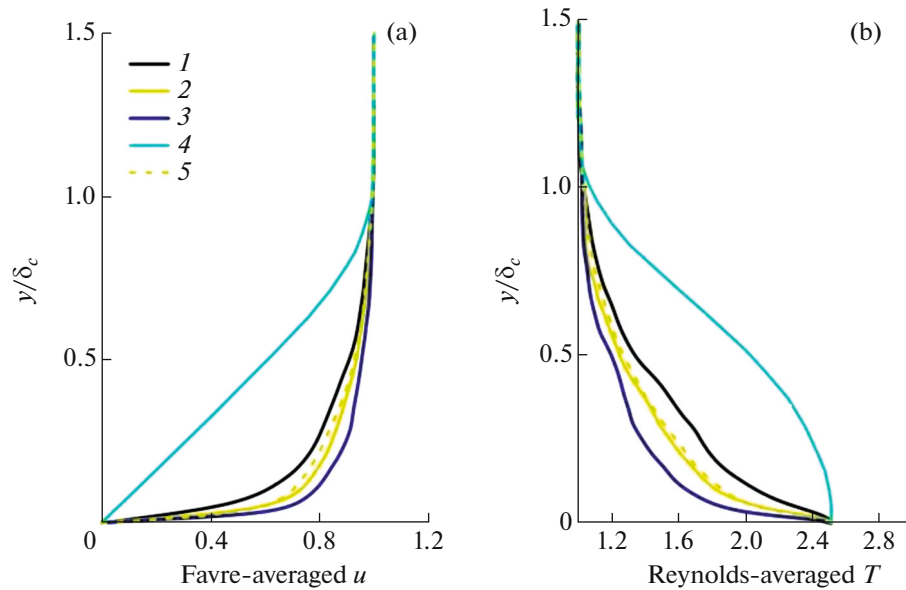
Fig. 13. (a) Favre-averaged streamwise velocity and (b) Reynolds-averaged temperature on the fine grid for (*1*) $x^* = 0.942$ m; (*2*) $x^* = 0.996$ m; (*3*) $x^* = 1.051$ m; (*4*) laminar boundary layer; and (*5*) work [1], $x^* = 0.996$ m.

Figure 13 shows averaged profiles of gasdynamic variables. The stronger the effect of nonlinear interactions in the considered section, the more convex the average profiles. Once again, the results produced by the dissipative scheme at $x^* = 0.996$ m agree well with those of [1]. Figure 13 confirms that, despite the insufficiently detailed pattern of small-scale vortices produced by the dissipative method, the integral flow characteristics (average profiles of gasdynamic variables, the average skin friction coefficient) are fairly similar to the results obtained with low-dissipative schemes [1]. This conclusion is important for applications that do not need a detailed resolution of all developed turbulent structures, but require reliable integral flow characteristics.

4. CONCLUSIONS

Dissipative numerical schemes are suitable for LTT simulation and reliable reproduction of integral flow characteristics, such as skin friction coefficients and average profiles of gasdynamic variables. This conclusion was confirmed by a detailed comparison of the present results with those produced by low-dissipative schemes [1].

The location of the LTT onset nearly does not depend on the number of grid nodes and the order of accuracy of the scheme when the fundamental harmonic and its nearest subharmonics are resolved sufficiently well. Apparently, the grid resolution of higher order harmonics plays a minor role in the simulation of the LTT onset and integral flow characteristics.

In the linear regime, the results based on the dissipative scheme agree well with those of [1]. In the developed nonlinear regime, the excessive dissipativity of the scheme can lead to an insufficiently detailed resolution of small-scale structures, which can be avoided by mesh refinement. To improve the accuracy of LTT simulation, the dissipativity of the scheme can be reduced in regions where this property is not required (for example, in boundary layers). This aspect will be the subject of further research.

REFERENCES

1. C. S. J. Mayer, D. A. V. Terzi, and H. F. Fasel, "DNS of complete transition to turbulence via oblique break-down at Mach 3," AIAA Paper No. 2008-4398 (2008).

2. I. V. Egorov, A. V. Novikov, and K. Kh. Din', "Direct numerical simulation of laminar–turbulent transition in supersonic flow over a sharp-edged plate," Uch. Zap. TsAGI **49** (5), 17−25 (2018).

3. I. V. Egorov and A. V. Novikov, "Direct numerical simulation of laminar–turbulent flow over a flat plate at hypersonic flow speeds," Comput. Math. Math. Phys. **56** (6), 1048−1064 (2016).

4. P. V. Chuvakhov, A. V. Fedorov, and A. O. Obraz, "Numerical simulation of turbulent spots generated by unstable wave packets in a hypersonic boundary layer," Computers Fluids **162**, 26−38 (2018).
https://doi.org/10.1016/j.compfluid.2017.12.001

5. C. S. J. Mayer, D. A. V. Terzi, and H. F. Fasel, "Direct numerical simulation of complete transition to turbulence via oblique breakdown at Mach 3," J. Fluid Mech. **674**, 5−42 (2011).

6. F. M. White, *Viscous Fluid Flow* (McGraw-Hill, New York, 1991).

Translated by I. Ruzanova